Advances in Applied Mathematics and Mechanics
Adv. Appl. Math. Mech., Vol. **18**, No. 1, pp. 67-92

DOI: 10.4208/aamm.OA-2024-0030
February 2026

# Numerical Investigation of Dynamics Stall on Vertical Axis Wind Turbine

Ao Zhang[1], Haocheng Yu[1], Jingzhou Zeng[2], Wei Zhao[2], Hao Wen[1] and Jianguo Zheng[1,*]

[1] *School of Aerospace Engineering, Huazhong University of Science and Technology, Wuhan, Hubei 430074, China*
[2] *Wuhan Second Ship Development Design Institute, Wuhan, Hubei 430064, China*

Received 7 February 2024; Accepted (in revised version) 17 March 2024

**Abstract.** Dynamic stall poses a significant aerodynamic challenge for vertical axis wind turbines (VAWTs) and serves as a key impediment to enhancing their overall efficiency. Consequently, to elucidate the underlying mechanism of dynamic stall and facilitate a clearer understanding of the entire dynamic stall process, a numerical investigation is conducted over the blades of a VAWT system. A two-dimensional numerical simulation is conducted by employing unsteady Reynolds-averaged Navier-Stokes (RANS) calculations with a Reynolds stress turbulence model. Four real-time key indicators are generalized to quantitatively characterize dynamic stall over the VAWTs. These indicators have been demonstrated to accurately predict the initiation and detachment times of the dynamic stall vortex (DSV), providing deeper insights into the underlying mechanism of DSV development. Additionally, this study explores the impact of blade thickness on the dynamic stall of VAWTs. Three airfoils from the NACA 4-digit series, each featuring distinct ratios of thickness to chord length, are examined. As the blade cross-section transitions from NACA 0012 to NACA 0015 and NACA 0018, heightened blade thickness results in a delayed onset of dynamic stall, shifting from leading edge stall to trailing edge stall. Moreover, the blade thickness significantly influences the efficiency of VAWT system, with increased airfoil thickness contributing to an improved utilization of wind energy.

**AMS subject classifications**: 76G25

**Key words**: Dynamics stall vortex, vertical axis wind turbines, blade thickness, leading-edge stall, trailing-edge stall.

## 1 Introduction

In recent years, due to environmental pollution, global warming and shortage of tradit-

*Corresponding author.
*Email:* zhengjg@hust.edu.cn (J. Zeng)

 

ional fossil energy, renewable energy such as solar energy, geothermal energy, biomass energy, wind energy, wave energy has been significantly developed. Among them, wind energy is one of the most promising energy sources in the renewable energy industry [1]. Wind power generation is currently the main form of utilizing wind energy. A wind turbine is a device that converts wind energy into mechanical work and then into electrical energy. Wind turbines typically consist of a tower, rotor, nacelle, and control systems. Wind turbines can be classified into two main types: horizontal axis wind turbines and vertical axis wind turbines. In a horizontal axis wind turbine (HAWT), the rotor rotates around a horizontal axis parallel to the ground. In contrast, a vertical axis wind turbine (VAWT) has a rotor that rotates around a vertical axis perpendicular to the ground. Each category of wind turbines possesses distinct advantages and is well-suited for specific applications [2].

Compared to HAWT, VAWT offers several advantages. Firstly, VAWT outperforms in low wind speed conditions owing to its lower cut-in wind speed, enabling it to commence operations at lower wind speeds. This makes VAWT more efficient in areas with lower average wind speeds. Secondly, VAWT's compact design allows for installation on rooftops or in other limited spaces, making it a preferred choice in urban and densely populated areas where HAWT installations are not suitable [3, 4]. Simultaneously, VAWT's vertical axis allows it to capture wind from any direction, making it well-suited for urban environments with irregular wind patterns [5]. Furthermore, VAWT can operate effectively in harsh conditions and is relatively easier to maintain compared to HAWT. In addition, VAWT can be integrated into hybrid renewable energy systems, working in conjunction with other energy sources such as solar panels or diesel generators, providing a more stable and reliable energy supply.

The efficiency of VAWT is directly impacted by its aerodynamic performance, which, in turn, is characterized by a rather complex set of aerodynamic features. As the blades of a VAWT rotate, they experience different wind speeds and angles of attack during each rotation. As shown in Fig. 1, the relative wind velocity $W$, which is the combination of the rotational velocity $\omega R$ and the freestream wind speed $U_\infty$, undergoes changes in magnitude and direction with the azimuth angle $\theta$. Consequently, the effective angle of attack (AoA) of the blades varies accordingly. Figs. 2(a) and (b) show the changes of effective AoA and relative wind velocity with azimuth angle for a blade-tip speed ratio (TSR) of 2. During blade rotation, the angle of attack exceeds the static stall angle of the airfoil within a specific azimuth angle range, causing the separation of airflow over the blades. Consequently, the flow over the blades alternates between an attached flow state and a stalled flow state throughout a rotation cycle, leading to dynamic stall [6]. Blade dynamic stall is a primary aerodynamic challenge faced by VAWT and constitutes a major obstacle to achieving higher efficiency in VAWT. More specifically, when the angle of attack of the airfoil changes rapidly, a shear layer near the leading edge (LE) of the airfoil rolls up and forms a leading-edge vortex (LEV), causing the airfoil suction surface to gain additional suction. As a result, airfoil's lift increases dramatically and stall is delayed. However, the leading-edge vortex quickly becomes unstable and detaches from

the suction side of the airfoil. With the detachment of the leading-edge vortex, the airfoil's lift rapidly decreases, and the pitching moment suddenly increases [7]. Therefore, in order to improve the power of VAWT, it is necessary to understand the dynamic stall phenomenon of VAWT.

It is widely accepted that the key factors influencing the aerodynamic characteristics of VAWT include blade geometric parameters, Reynolds number, blade number, blade tip speed ratio, and other related variables. Currently, there is limited research on the impact of blade thickness on VAWT dynamic stall. Benton and Visbal studied four different NACA series airfoils, namely 0009, 23009, 0012 and 23012, to observe the effect of changing the leading-edge radius and blade thickness of the airfoil on dynamic stall at Reynolds number (Re) of $2\times10^5$ [8]. They observed that the laminar separation bubble (LSB) gradually reduced in size as the airfoil AoA increased. However, the substantial radius of the leading edge of the NACA 23012 airfoil prevented the rupture of the LSB under the influence of the pressure gradient. However, the pressure-induced rupture of LSB can be observed for other airfoils. Sharma and Visbal used large eddy simulation (LES) to study the influence of airfoil thickness (9%, 12%, 15% and 18% of the chord length) on the dynamic stall initiation mechanism of an oscillating airfoil at Re$=2\times10^5$ [9]. In all the cases, the LSB is followed by the formation of dynamic stall vortex (DSV). In the case of NACA 0009 airfoil, it is found that the separation of turbulent boundary layer does not occurs at the trailing edge (TE) of the airfoil. For NACA 0018 airfoil, the separation region extends from the trailing edge of the airfoil to the LSB region before the stall occurs, suggesting that the dynamic stall may be caused by the interaction between turbulent boundary layer and LSB. In the other three cases, the stall is caused by the pressure-induced LSB rupture. Ouro et al. conducted a large eddy simulation study on the NACA 0012 and NACA 4412 airfoils, and observed that in the early pitch stage, several small vortices formed on the suction surface of the airfoil, and these vortices eventually gathered near the leading edge to form a leading-edge vortex [10]. In the case of NACA 0012 airfoil, the leading-edge vortex forms earlier, while in the case of NACA 4412 airfoil, due to its larger curvature radius, the clinging time is longer.

The review of the existing literature reveals a scarcity of research on exploring the influence of airfoil thickness on the dynamic stall of VAWT blades. Moreover, current studies lack a comprehensive visualization and description of the dynamic stall vortex from a quantitative perspective, including its initiation and detachment. The complete mechanism underlying the occurrence of dynamic stall remains inadequately elucidated. In this context, our work is structured around two primary objectives. Firstly, we perform a quantitative analysis of the VAWT dynamic stall process, utilizing critical indicators of flow characteristics to enhance our understanding of the entire dynamic stall process. Secondly, we aim to investigate the impact of airfoil thickness on the dynamic stall process, aiming to unveil the underlying mechanism of dynamic stall.

This paper is organized as follows: in Section 2, the physical model and numerical method will be described. The results are presented and analyzed in Section 3. Finally, the main findings of this study are summarized in Section 4.

# 2 Physical model and numerical method

## 2.1 VAWT model and operational parameters

This study employs a two-dimensional H-type VAWT model with two blades, as shown in Fig. 1. The geometrical and operational parameters of the VAWT are presented in Table 1. The VAWT has a radius of $R=0.25$m, and uses NACA 4-digit symmetric airfoils with a chord length of $c=0.15$m as the cross-sections of the rotating blades. The airfoil profiles considered in the present study with different thickness are shown in Fig. 3. The blade tip speed ratio is denoted as $\lambda=\omega R/U_\infty$ with the angular speed of the blade represented by $\omega$ and freestream velocity by $U_\infty$, respectively. The angle of attack, denoted as $\alpha$ and depicted in Fig. 2, is a function of the azimuth angle $\theta$,

$$\alpha=\arctan\Big(\frac{\sin\theta}{\lambda+\cos\theta}\Big). \tag{2.1}$$

The relative wind speed is defined as,

$$W=U_\infty\sqrt{\sin^2\theta+(\lambda+\cos\theta)^2}. \tag{2.2}$$

We use the torque coefficient $C_Q$ and the power coefficient $C_p$ to evaluate the aerodynamic efficiency of VAWT, which provides a convenient metric for different VAWT. They are defined as follows,

$$C_Q=\frac{T}{1/2\rho U_\infty^2 AR}, \tag{2.3a}$$

$$C_p=\frac{T\omega}{1/2\rho U_\infty^3 A}, \tag{2.3b}$$

where $T$ denotes the torque of the blades and $A$ is the vertical cross-sectional area of the turbine. In our 2D simulation, $A$ takes the value of the rotor diameter.

Table 1: Geometrical and operational parameters of the VAWT.

| Characteristics | Turbine |
|---|---|
| Airfoil | NACA 0012, NACA 0015, NACA 0018 |
| Number of blades $n$ | 2 |
| Chord length $c$ | 0.15m |
| Strut position $S$ | 0.25c |
| Fixed pitch angle $\beta$ | $0^\circ$ |
| Rotation diameter $D$ | 0.5m |
| Freestream velocity $U_\infty$ | 6.54m/s |
| Rotational speed $\Omega$ | 3000deg/s |
| Tip Speed Ratio (TSR) $\lambda$ | 2 |

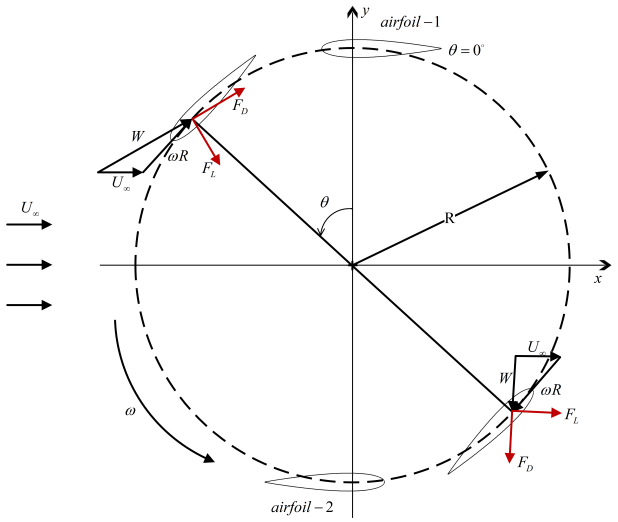


Figure 1: Velocity and force vectors around the blades in a H-type two-blade VAWT model.

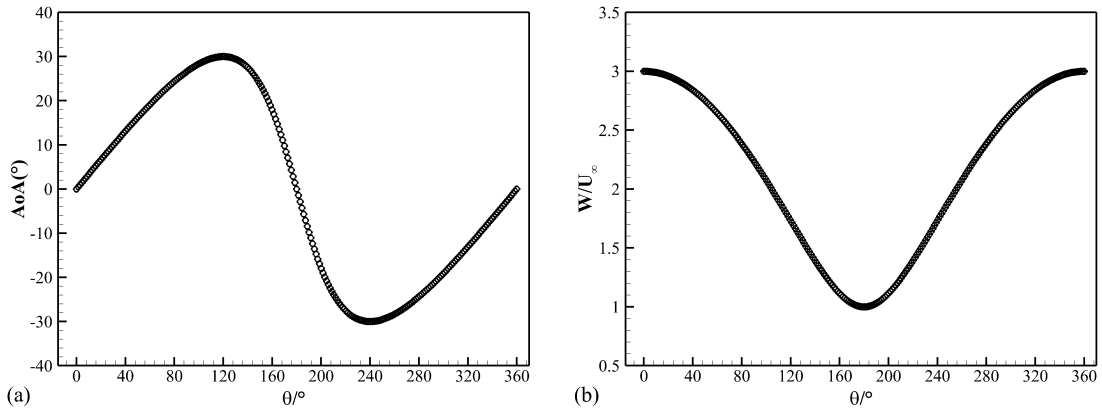


Figure 2: The variations of the angle of attack (a) and relative wind velocity (b) with the azimuth angle under TSR $=2$ for a VAWT blade.

## 2.2 Unsteady Reynolds-averaged Navier-Stokes equations

The airflow around the VAWT blades is assumed to be fully turbulent, and is governed by unsteady Reynolds-averaged Navier-Stokes (URANS) equations,

$$\frac{\partial \rho}{\partial t}+\frac{\partial}{\partial x_i}(\rho v_i)=0, \tag{2.4a}$$

$$\frac{\partial}{\partial t}(\rho v_i)+\frac{\partial}{\partial x_j}(\rho v_j v_i)=-\frac{\partial p}{\partial x_i}+\frac{\partial}{\partial x_j}(\tau_{ij}-\rho\overline{v_i'' v_j''}), \tag{2.4b}$$

$$\begin{aligned}\frac{\partial}{\partial t}(\rho E)+\frac{\partial}{\partial x_j}(\rho v_j H)=&\frac{\partial}{\partial x_j}\left(\kappa\frac{\partial T}{\partial x_j}-\rho\overline{v_j'' h''}+\overline{\tau_{ij} v_i''}-\frac{1}{2}\rho\overline{v_j'' v_k'' v_k''}\right)\\&+\frac{\partial}{\partial x_j}\left[v_i(\tau_{ij}-\rho\overline{v_i'' v_j''})\right],\end{aligned} \tag{2.4c}$$

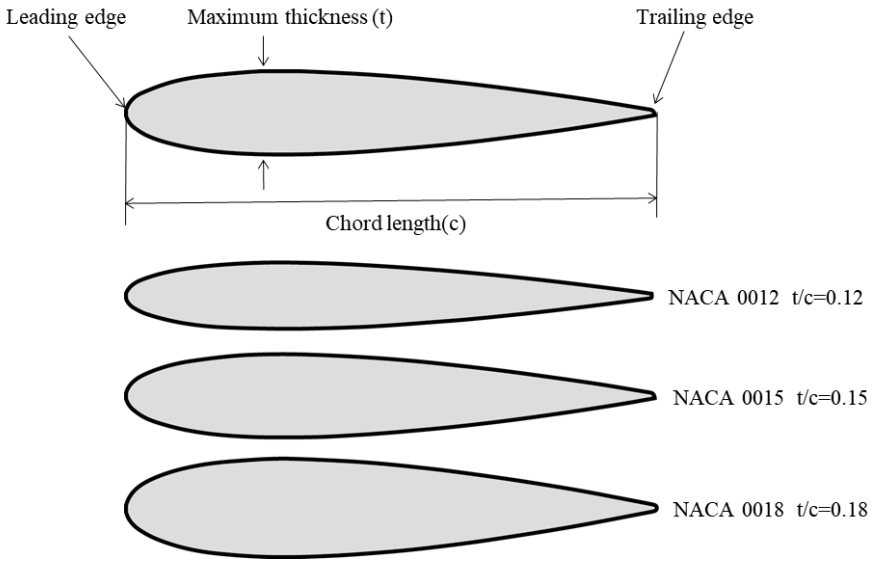


Figure 3: NACA 4-digit symmetric airfoils considered in this study.

In the above set of equations, the flow variables $\rho$, $p$, $T$, $v_i$ and $\tau_{ij}$ denote the mean density, pressure, temperature, velocity components in $x_i$ coordinates and viscous stress tensor, respectively. The variables with double prime $''$ denote turbulent fluctuations, while $-$ denotes Reynolds averaging. The total energy $E$ and enthalpy $H$ are given by $E=e+v_iv_i/2+k$ and $H=e+p/\rho+v_iv_i/2+k$, respectively, where $e$ is the internal energy per unit mass, and k is the turbulent kinetic energy, defined as $k=\overline{v_i''v_i''}/2$. To close the above system, the Reynolds stress tensor $\tau_{ij}^R=-\rho\overline{v_i''v_j''}$ must be determined. In this study, a sophisticated Reynolds stress turbulence model (RSM) is used with $\tau_{ij}^R$ computed by solving the Reynolds stress transport equations. The validity of the RSM model in predicting shear-layer separation and flow reattachment has been extensively validated [11]. In addition, perfect gas equation of state (EOS), $p=\rho RT$, is used to model airflow, with the gas constant taking the value of $R=287J/(Kg\cdot K)$.

## 2.3 Numerical setup and mesh generation

In this study, we employ two-dimensional (2D) numerical simulations to analyze the flow patterns around the blades of a wind turbine. The computational domain, illustrated in Fig. 4, is a rectangular region with dimensions of $D\times 2.5D$, where $D$ equals 4m. This domain is partitioned into two distinct sections: a rotating inner subdomain characterized by a radius of $1.6R$ and a stationary outer subdomain. The two subdomains are interconnected through an interface. Regarding the boundary conditions, the left boundary of the outer domain is defined as a velocity inlet boundary, the right boundary is

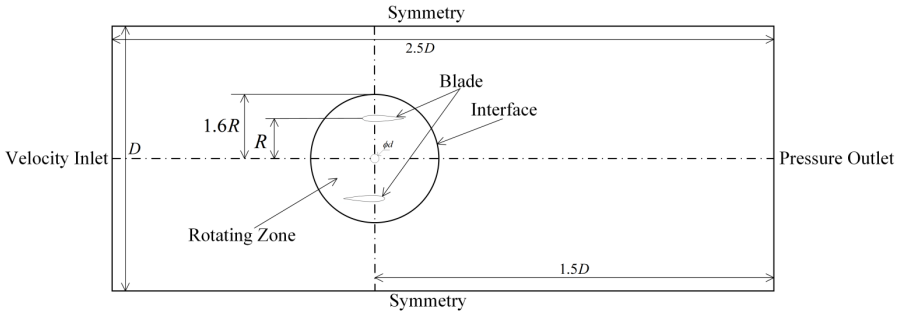


Figure 4: The diagram of computation domain.

set as a pressure outlet, and the upper and lower boundaries are specified as symmetric boundaries [12]. To enhance the realism of the VAWT simulation, a rod with a diameter of $d = 0.02$m is introduced at the center of the rotating subdomain to emulate the rotational axis of the wind turbine. The computational domain is discretized using a hybrid mesh, as illustrated in Figs. 5(a)-(c). In regions proximate to the blades and rod, a structured grid is employed, ensuring good orthogonality and refinement near the solid walls to achieve a target wall-normal spacing of $y^+ = 1$ in the first mesh layer adjacent to the walls. This treatment enhances calculation accuracy in the near-wall region of the blades, facilitating a more precise resolution of viscous effects. Simultaneously, unstructured grid is created to encompass the remaining portion of the rotating subdomain. The outer subdomain is also covered by a structured grid. The total grid count amounts to approximately 900,000.

The system of Eq. (2.4) is solved by employing a cell-centered finite volume method. Discretization of the pressure and convective terms is achieved through a second-order upwind scheme. For unsteady simulation, a dual-time-stepping methodology is applied during time-marching. To enhance solution convergence, a multi-grid technique is incorporated. In the choice of the time step, a rotation of $0.006^\circ$ is implemented for each time step, ensuring a balance between numerical simulation accuracy and computational efficiency.

## 2.4 Verification and validation of the numerical method

### 2.4.1 Validation of the numerical method

To assess the accuracy of the employed numerical approach, a validation study was undertaken, utilizing data from the experiment and simulation conducted by Li et al. [13]. The experiment reported in the reference was conducted in an open jet wind tunnel on a VAWT model. The wind turbine has two blades with a NACA 0015 airfoil for its blade cross-section. The blade specifications include a chord length of 0.225m, a blade span of 1.02m, a blade pitch angle set at $6^\circ$, and a wind turbine rotation radius of 0.85m. The

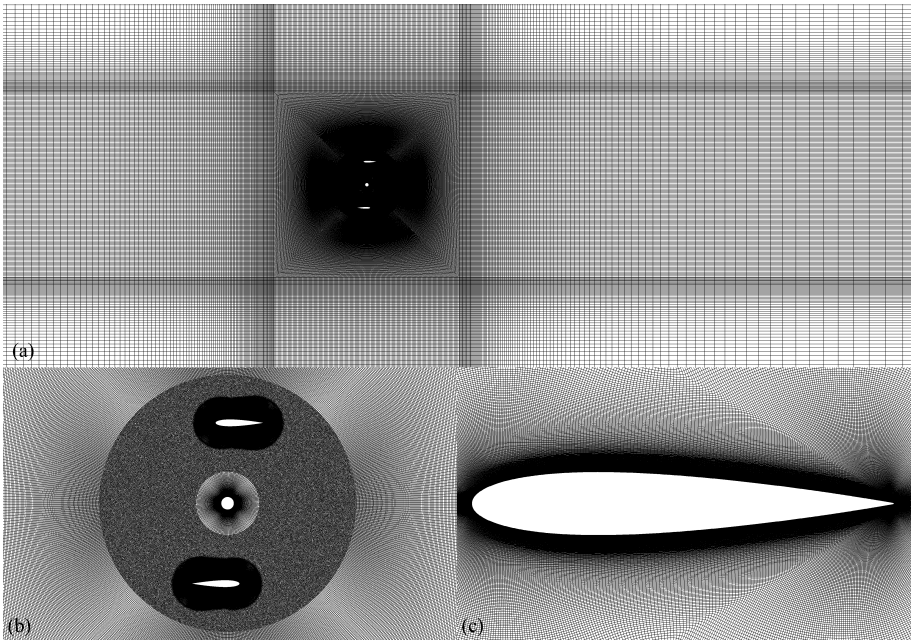


Figure 5: The global view of grid (a), and local view of grid (b)-(c).

freestream flow velocity is maintained at 7m/s, resulting in a tip speed ratio of 2.29 and a chord-length-based Reynolds number of $2.89\times10^5$. We reproduced the experimental conditions and performed a simulation with identical physical parameters. In Fig. 6, a numerical representation of the instantaneous vorticity field from our simulation is illustrated. As depicted in Fig. 6, vortices consistently shed from the rotating blades, traverse downstream under the influence of the freestream, and create a distinct wake. Clearly, our numerical simulation accurately reproduces key flow characteristics of the VAWT, such as the vortex core and its trajectory. The resolved flow pattern demonstrates a noteworthy qualitative agreement with the experimental flow pattern documented in the literature, say that seen in reference [14].

In addition, in Fig. 7, the curve representing the phase-averaged moment coefficient of the VAWT from our simulation is compared with the corresponding data from the experiment and simulation presented in [13]. Our numerical results exhibit strong concordance with the experimental data concerning the overall trend of the moment coefficient relative to the azimuth angle. Remarkably, within the azimuth angle range of 180-360°, our numerical curve closely follows the experimental one, demonstrating exceptional agreement. In contrast, the numerical data from reference [13] deviates significantly from the experimental curve. However, during the initial half of the rotation cycle, spanning the azimuth angle from 0 to 180°, disparities between our simulation and the experiment in [13] become apparent. The moment coefficient is consistently either overpredicted or underpredicted relative to the experimental data. It is crucial to highlight that this par-

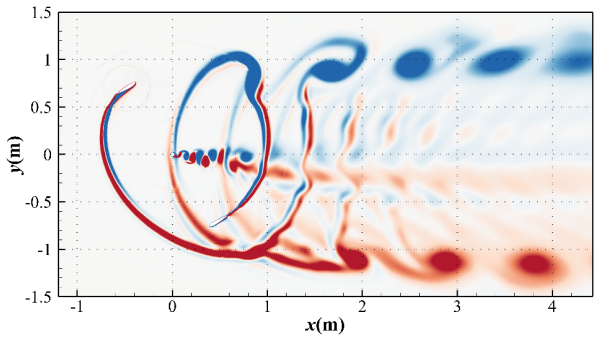


Figure 6: The instantaneous vorticity field from our simulation for the VAWT model from reference [13].

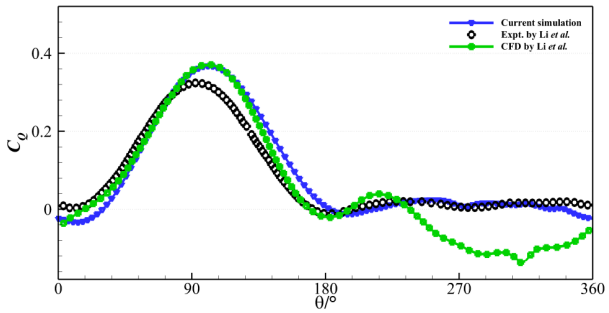


Figure 7: Comparison of the variation of phase-averaged moment coefficient with azimuth angle between our simulation and the experiment conducted by Li et al. [13].

ticular azimuth angle range is marked by severe dynamic stall, a phenomenon posing a considerable challenge for accurate prediction in computational fluid dynamic simulations, irrespective of turbulence models employed. Despite the challenges inherent in predicting dynamic stall, our thorough verifications confirm that our numerical simulation aligns closely with the experimental results, capturing both the qualitative flow structures and the quantitative variations in aerodynamic coefficient. Consequently, it is reasonable to assert that our numerical method is dependable.

## 2.5 Validation of the grid independence

During the operation of vertical axis wind turbines, vortical structures with significant characteristic scales are generated around the airfoil. To ensure that the complex vortex structures are properly resolved, a grid independence verification was conducted in this section to ensure the accuracy of the numerical simulation results. Three different densities of computational grids were generated for verification (coarse grids: $4.2\times10^5$; medium grids: $9.5\times10^5$; fine grids: $5.0\times10^6$). The curves of the instantaneous torque coefficient of a single blade predicted by these three sets of grids are shown in Fig. 8. It

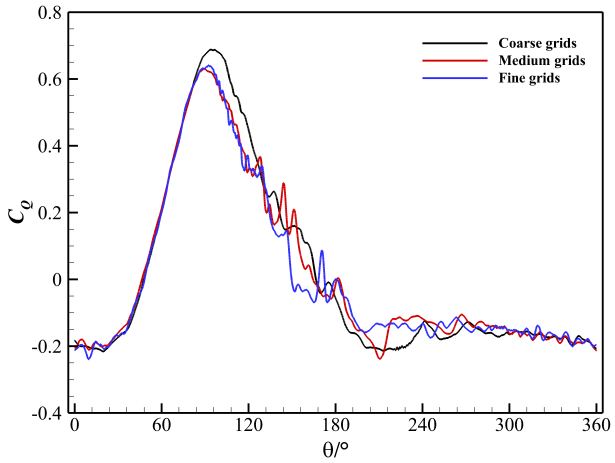


Figure 8: The instantaneous moment coefficient predicted with coarse, medium, and fine grids ($\lambda = 2.0$ and $U_\infty = 6.544984\text{m/s}$).

is clear from the figure that the medium and fine grids have similar predictions, while the results predicted by the coarse grid, although showing a similar trend, have significant numerical differences, especially between azimuth angles of 90 and 240. This indicates that the coarse grid cannot accurately predict the flow characteristics of vertical axis wind turbines during operation, while the medium and fine grids can simulate them well. Therefore, for efficient simulation, the medium grid will be used in subsequent simulations.

# 3 Results and discussion

## 3.1 Dynamic stall over VAWT blades

In this section, we initially examine a VAWT featuring the cross-sectional shape of NACA 0015 airfoil to elucidate its fundamental flow characteristics. With a VAWT tip speed ratio of 2 and a rotational speed of 3000deg/s, the freestream velocity is calculated to be 6.54m/s. During the operation of the VAWT, as the blade azimuth angle changes, the effective angle of attack also varies. This process results in the onset of unstable dynamic stall. Within the realm of deep dynamic stall, the emergence of large-scale leading-edge vortices (LEV), also referred to as dynamic stall vortices, represents a crucial and noteworthy phenomenon. Typically, the presence of dynamic stall vortices induces an instantaneous lift overshoot and stall delay. However, as these vortices move rearward, they prompt rapid fluctuations in pitching moment, potentially leading to negative damping and flutter [15]. Moreover, the detachment of the DSV further results in a large flow separation on the blade surface, thus producing a sharp drop in lift. To unveil the flow

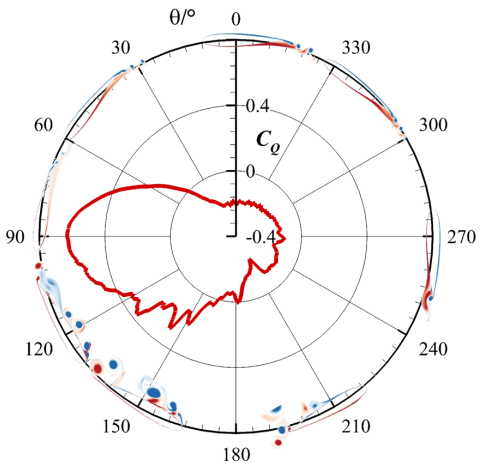


Figure 9: The instantaneous moment coefficient $C_Q$ of a VAWT blade and the representative vorticity field in a revolution cycle. $\lambda=2.0$ and $U_\infty=6.544984$m/s.

mechanisms associated with phenomena in the deep dynamic stall regime and enhance flow control, it is imperative to delve into the physical processes governing the initiation, development, and detachment of DSV.

Fig. 9 shows the instantaneous torque coefficient of a single blade over a revolution cycle and its representative vorticity field. It can be observed from the figure that at the start of the wind turbine operation from $\theta=0^\circ$, as the azimuth angle increases, the torque coefficient steadily rises, with the airflow fully adhering to the airfoil surface. However, after the azimuth angle reaches $90^\circ$, the torque coefficient rapidly decreases and oscillates sharply. This occurs because the continuous increase in the azimuth angle causes the airfoil's angle of attack to surpass the stall angle, resulting in dynamic stall. When the azimuth angle reaches $164^\circ$, the torque coefficient becomes negative. At an azimuth angle of $180^\circ$, the angle of attack of the airfoil decreases to $0^\circ$, and the airflow begins to reattach locally in the leading-edge area of the airfoil. Subsequently, as the airfoil moves from the windward to the leeward side, only a slight dynamic stall occurs, which is evident from the changes in both the vorticity map and torque coefficient.

During the dynamic stall process, various flow structures leave pressure footprints on the blade surface, which can be used to understand the development of different flow phases and predict critical flow events. In this study, a criterion for identifying dynamic stall vortex over a pitching airfoil is generalized to the current VAWT flow. It utilizes blade suction surface pressure to establish key indicators predicting flow events associated with dynamic stall vortices [16]. These indicators include: (I) the spatial distribution coefficient of pressure (SDCP); (II) the high-order central moment of pressure (HCMP); (III) the location of peak pressure (LPP); (IV) the modulated location of peak pressure (MLPP). Among them, SDCP and HCMP are used to predict DSV initiation, while LPP

and MLPP is used to predict DSV detachment. As will be seen later, the critical indicators used in this study demonstrate accurate prediction of significant flow events during the dynamic stall process. They serve as a valuable reference for quantitatively identifying the times when DSV initiation and detachment occur.

### 3.1.1 The criteria for detecting DSV initiation

The data necessary for calculating SDCP, HCMP, LPP, and MLPP is collected first. As the suction surface of the airfoil undergoes periodic changes during the wind turbine's operation, data is selectively sampled from the suction surface during the first half of a revolution cycle ($0^\circ-180^\circ$). Assume that there are $N_s$ pressure transducers placed along the suction surface of the airfoil, starting from the leading edge and extending to the trailing edge. These transducers are labeled with serial numbers ranging from $n=1$ to $N_s$. The pressure coefficient of the $n$th transducer at time $t^*$ is represented as $C_{p,n}(t^*)$, and its chordwise dimensionless coordinate is denoted as ${x_n}^*$, where $t^*=tU_\infty/c$, ${x_n}^*=x_n/c$. In this context, the spatial distribution coefficient of pressure can be defined as follows:

$$\begin{aligned}\mathrm{SDCP}(t^*)=&\sum_{n=1}^{N_s-1}[C_{p,n+1}(t^*)-C_{p,n}(t^*)]\\&\times(1-{x_n}^*)^{\mathrm{sgn}(C_{p,n+1}(t^*)-C_{p,n}(t^*))}{x_n}^{*[1-\mathrm{sgn}(C_{p,n+1}(t^*)-C_{p,n}(t^*))]},\end{aligned}\tag{3.1}$$

where sgn is the standard symbolic function, which is defined as,

$$\mathrm{sgn}(x)=\begin{cases}1, & \text{if } x\geq 0,\\ 0, & \text{if } x<0.\end{cases}\tag{3.2}$$

Meanwhile, the occurrence of the critical flow event can also be predicted by measuring the change of pressure coefficient using statistical quantities. In the calculation of HCMP, the pressure coefficient data of different spatial measurement points are used, and the mathematical definition of HCMP is as follows,

$$\mathrm{HCMP}(t^*)=\frac{1}{N_s}\sum_{n=1}^{N_s}\{[-C_{p,n}(t^*)]-[-\overline{C_p(t^*)}]\}^m,\tag{3.3}$$

where $m$ is the order of the moment, prescribing that $m\in N^+$, and $m>1$. In Eq. (3.3), $\overline{C_p(t^*)}$ represents the average value of the pressure coefficient from all pressure transducers at a certain time,

$$\overline{C_p(t^*)}=\frac{1}{N_s}\sum_{n=1}^{N_s}C_{p,n}(t^*).\tag{3.4}$$

Subsequently, criteria SDCP and HCMP are employed for a quantitative analysis of the development of dynamic stall vortex over the VAWT. Fig. 10 illustrates the temporal variation curves of SDCP and HCMP during the initial half of the VAWT blade revolution.

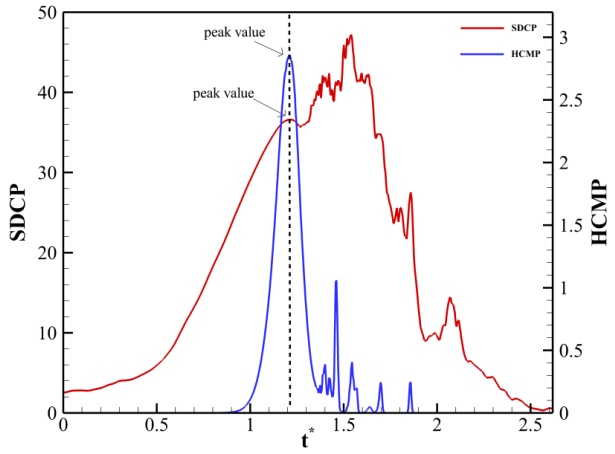


Figure 10: Temporal evolution plots of SDCP and HCMP during the initial half of the blade revolution.

Observing the two curves, it is evident that they share a common peak value at $t^*=1.213$. Correspondingly, the airfoil attains an azimuth angle of 83.4° and an angle of attack of 25.1592°, signifying the initiation of the dynamic stall vortex. This particular time is henceforth defined as $t_1$. The flow field at time $t_1$ is depicted in Fig. 11. It is evident that the dynamic stall vortex manifests in the airfoil's leading-edge region, roughly between $x/c=0.01$ and 0.06. It is important to note that all the flow field images presented in this paper have been retroactively rotated to the initial position at $\theta=0°$ for ease of observation. This consideration should be kept in mind while interpreting and comprehending the results.

Alternatively, the commencement of the dynamic stall vortex can be confirmed by examining the skin friction coefficient $c_f$. Following the description by Narsipur et al. [17], the occurrence of the inflection point for the first time within the negative-value region of the $c_f$ profile along the suction surface of the blade aligns with the initiation of the DSV. Fig. 12 illustrates the $c_f$ curve, highlighting the initial appearance of inflection point within the negative $c_f$ region. The specific time instant associated with the $c_f$ curve, corresponds to the time instant determined by the SDCP and HCMP methods mentioned earlier, i.e., $t^*=1.213$. Observing Fig. 12, it is evident that the DSV occupies the region approximately from $x/c=0.01$ to 0.06, aligning with the DSV region observed in the flow field presented in Fig. 10. Consequently, the initiation time of DSV is accurately determined through the use of SDCP, HCMP, and $c_f$.

### 3.1.2 The criteria for detecting DSV detachment

In addition to the formation of the DSV, another important critical event is the detachment of the DSV. DSV detachment refers to the process wherein the dynamic stall vortex separates from the blade surface and sheds downstream [16]. After its initiation, the

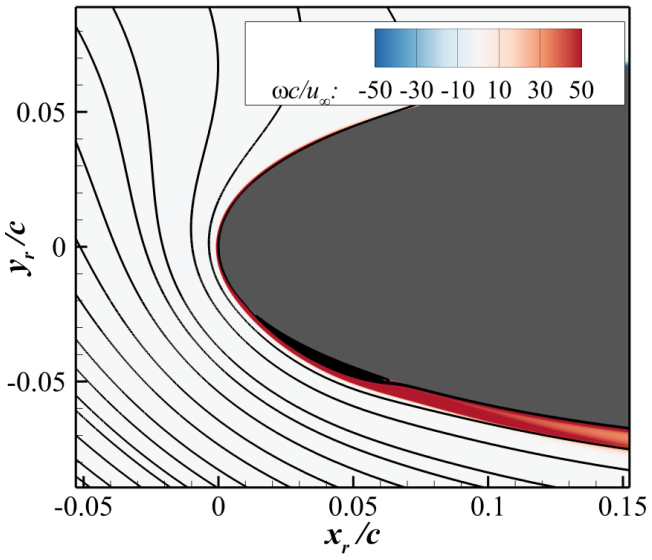


Figure 11: Transient flow field at time $t_1$ showing the initiation of dynamic stall vortex. The azimuth angle is $\theta = 83.4^\circ$.

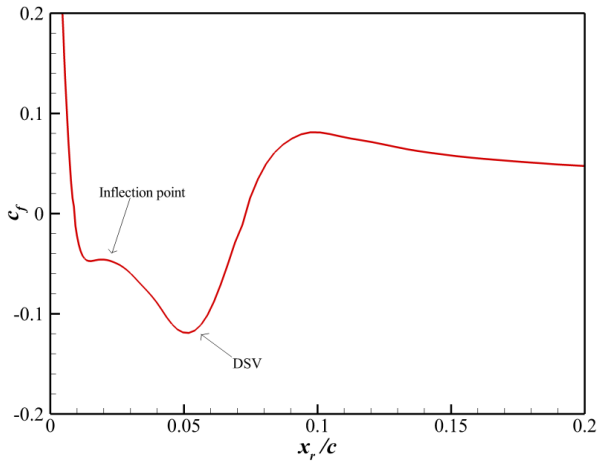


Figure 12: The curve of $c_f$ along the suction surface of the airfoil at time $t^* = 1.213$.

dynamic stall vortex experiences continuous growth and downstream convection. Monitoring the DSV's evolution during this convection process can be achieved by observing the pressure imprint it leaves on the surface. The most notable indication of the DSV's presence on the surface during convection is the existence of a distinct pressure wave [16]. Therefore, utilizing the pressure wave serves as a viable method for monitoring the DSV's state during the convection process and the associated critical events.

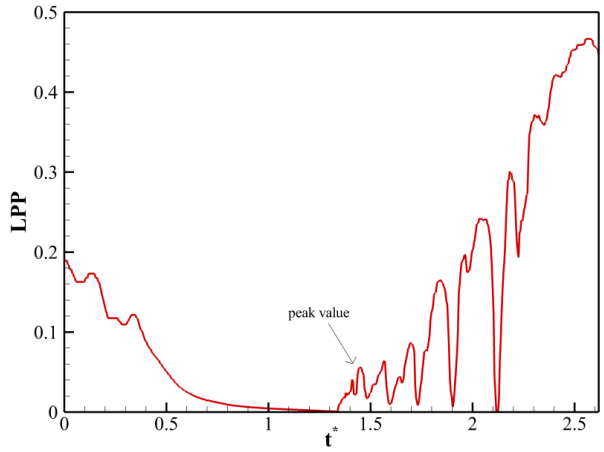


Figure 13: The time history of LPP.

For continuous real-time monitoring of the pressure wave position using pressure transducers, we introduce a straightforward definition here. The LPP is defined as the weighted average chordwise coordinates of the 10% measurement points with the most substantial negative pressure at each time. The selection of the 10% measurement points relies on an estimation of the spatial extent influenced by the negative pressure wave generated by the DSV. For the three different thickness airfoils studied in this paper, I used 6%, 8%, 10%, 12%, and 14% of points to calculate the LPP curves for each airfoil. The results show that while the numerical values of LPP change with the number of points, the characteristic values in the curves do not change significantly. This indicates that these slight variations do not affect the effectiveness of LPP. Therefore, in this paper, I uniformly use 10% of the points to calculate LPP. Assume that at time $t^*$ the serial number of the 10% transducers with the strongest negative pressure on the suction surface is $n=1,2,3,\cdots,N_{\max}10\%$, where $N_{\max}10\%$ is equal to the rounding of $N_s\times 10\%$, then the mathematical expression of LPP is given by,

$$\mathrm{LPP}(t^*)=\frac{\sum_{n=1}^{N_{\max 10\%}} C_{p,n}(x_n^*,t^*)x_n^*}{\sum_{n=1}^{N_{\max 10\%}} C_{p,n}(x_n^*,t^*)}. \tag{3.5}$$

Fig. 13 displays the time history of LPP during the initial half of the blade revolution. The first peak of LPP following the onset of the DSV is identified as the time of DSV detachment. In the figure, the time corresponding to the detachment point is $t^*=1.449$, with the airfoil having an azimuth angle of 99.6° and an angle of attack of 28.2734°. At time $t_1$, LPP exhibits a small value due to the presence of the leading-edge negative peak pressure. Subsequently, with the additional vorticity supplied by the shear layer, the circulation and size of the DSV experience a substantial increase, and the core of the DSV moves downstream, which results in an increase of the LPP value. As depicted in Fig. 13,

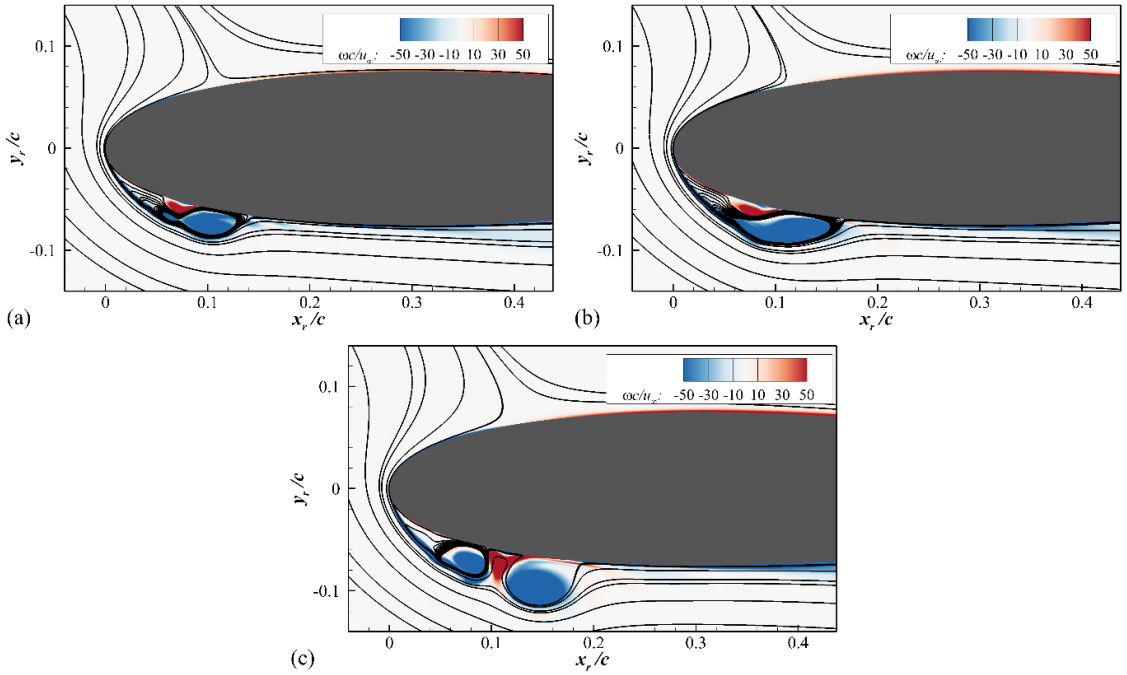


Figure 14: Vorticity contours around the airfoil at several times: (a) $t^*=1.405$, (b) $t^*=1.449$, (c) $t^*=1.492$.

after rising for a period of time, the value of LPP fell for a period of time. This is because the DSV continues to move downstream after separation, the surface negative pressure caused by the DSV decreases rapidly as the DSV moves away from the airfoil. At the same time, the newly generated DSV once again induces the strongest negative pressure near the leading edge, causing the LPP value to decrease.

Fig. 14 illustrates vorticity contours at three typical times: before, at, and after the detachment of the DSV. At $t^*=1.405$ (Fig. 14(a)), the vorticity contour reveals that the leading-edge shear layer continues to supply vorticity to the growing DSV, and the DSV has not yet been pinched off from the leading-edge shear layer. At $t^*=1.449$ (Fig. 14(b)), the DSV is in the process of being pinched off, most of the vorticity from the leading-edge shear layer is fed into the newly formed DSV and the secondary vorticity is erupting rapidly. At $t^*=1.492$ (Fig. 14(c)), the DSV has been pinched off from the leading-edge shear layer and begins to convect downstream. Subsequently, the DSV moves away from the airfoil surface after detachment, and its strength gradually diminishes. Based on these observations, $t^*=1.449$ can indeed be considered as the time for the detachment of the DSV in this case. In subsequent discussions, this reference time for DSV detachment is designated as $t_2$.

While the variation in LPP effectively indicates the criticality of DSV detachment, for a clearer identification of the $t_2$ time, further modulation of LPP can be applied to

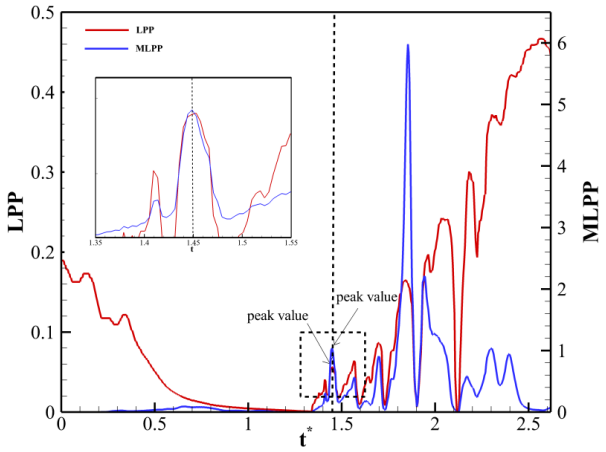


Figure 15: The LPP and MLPP curves.

accentuate its peak value at $t_2$. The root-mean-square of pressure coefficient $C_{p,RMS}$ used in this study is,

$$C_{p,RMS}(x^*,t^*)=\sqrt{\frac{1}{\Delta t^*}\int_{t^*-\Delta t^*}^{t^*}\left[C_p(x^*,t^*)-\overline{C_p(x^*,t^*)}\right]^2 \mathrm{d}t^*}, \tag{3.6}$$

where $\overline{C_p(x^*,t^*)}$ is the average value of the pressure coefficient at $x^*$ the period of $\Delta t^*$. Here, $\Delta t^*=4$ is the dimensionless time interval defining the filtering process. Eq. 3.6 follows the definition by Benard et al. [18]. In this definition, the calculation of $C_{p,RMS}$ only needs the historical value and current value of the surface pressure at a particular time, enabling real-time computation. Then, the LPP can be modulated by $C_{p,RMS}$ to obtain the MLPP,

$$\mathrm{MLPP}(t^*)=LPP(t^*)\times\sum_{n=1}^{Ns}\left[C_{p,RMS}(x_n^*,t^*)\right]^m, \tag{3.7}$$

where the $m$-th power of $C_{p,RMS}$ is used to modulate the LPP and the power exponent $m$ is an empirical parameter to control the degree of modulation. In this study, $m$ is consistently set to 3 across all cases. Fig. 15 illustrates the variation of LPP and MLPP. Following modulation, the peak value of MLPP at $t_2$ aligns with LPP but is more pronounced, facilitating more accurate identification of the DSV detachment. Consequently, predicting DSV detachment using MLPP is deemed feasible.

In summary, the successful generalization of the four indicators mentioned above to the analysis of VAWT flow facilitates the quantitative identification of the two critical events associated with the dynamic stall vortex: the initiation and detachment of DSV. This in turn contributes to a deeper understanding of physics of DSV dominating VAWT flow.

### 3.1.3 Influence of dynamic stall on aerodynamic performance of VAWT

Fig. 16 shows the variation of the instantaneous moment coefficient of the single blade/airfoil in one revolution cycle. It can be observed from the figure that the instantaneous moment coefficient is positive when the airfoil azimuth angle falls within the range of 46° to 164°. The corresponding angle of attack gradually increases from 15° to 30° and then decreases to 15°. This occurs because, at the onset of the flow, the airflow adheres closely to the airfoil surface, experiencing only minimal separation at the trailing edge of the airfoil. As the azimuth angle increases, the instantaneous moment coefficient rises rapidly and reaches the maximum value at the azimuth angle of 90°, aligning with the time when the DSV emerges at the leading edge of the airfoil suction surface. Subsequently, as the angle of attack continues to rise, the airfoil undergoes dynamic stall, leading to a swift reduction in the instantaneous moment coefficient.

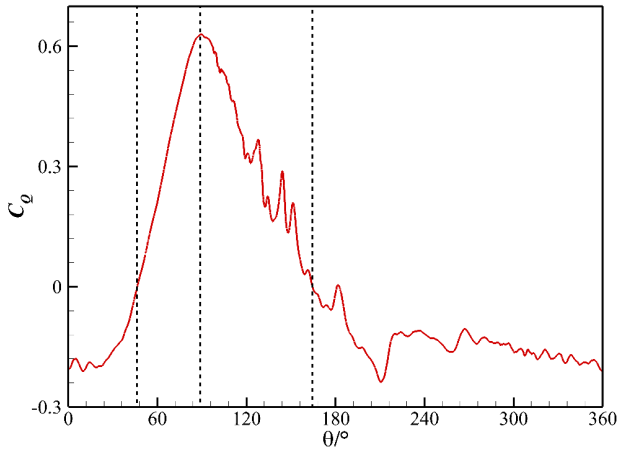


Figure 16: The variation of instantaneous moment coefficient of a single blade (NACA 0015 airfoil) in one revolution cycle.

## 3.2 Influence of airfoil thickness on dynamic stall

This section investigates the impact of airfoil thickness on dynamic stall. Three airfoils, namely NACA 0012, NACA 0015, and NACA 0018, are analyzed. Remember that for the NACA 0015 airfoil, the initiation and detachment times of DSV are $t^* = 1.213, 1.449$, respectively. The transient flow fields associated with the three airfoils are compared in Fig. 17 at the two critical times of the DSV over the NACA 0015 airfoil. In the first column of Fig. 17, the vorticity fields for the three airfoils are contrasted at time $t^* = 1.213$, while in the second column of Fig. 17, the comparison is made at time $t^* = 1.449$. Examining the first column of Fig. 17 reveals that upon the emergence of a new DSV at the leading edge of the NACA 0015 airfoil, a comparable DSV has already manifested and detached

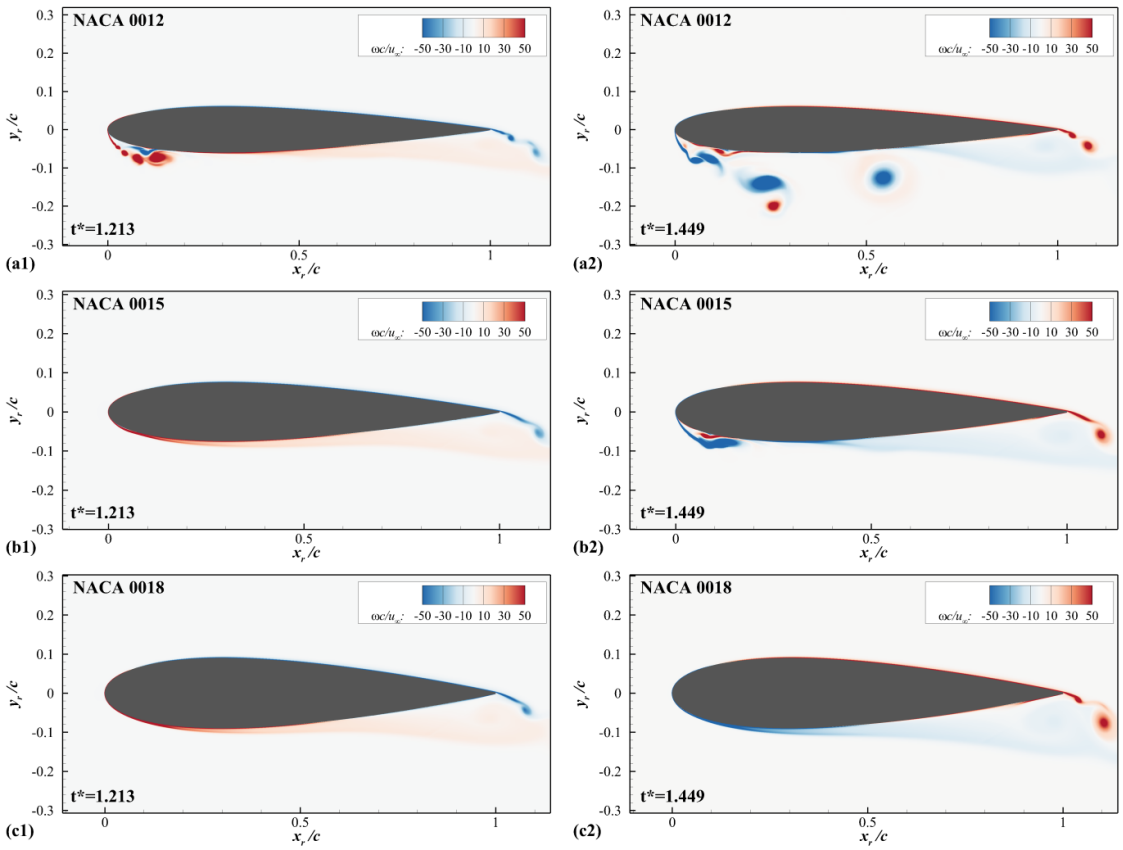


Figure 17: Comparison of the transient vorticity fields of NACA 0012 (a1)-(a2), NACA 0015 (b1)-(b2) and NACA 0018 (c1)-(c2) blades. The left and right columns correspond to time $t^* = 1.213, 1.449$, respectively.

from the surface of the NACA 0012 airfoil. In contrast, the DSV has not yet appeared on the thicker NACA 0018 airfoil. At time $t^* = 1.449$, the DSV begins to detach from the NACA 0015 airfoil. However, no discernible flow separation is observed in the leading-edge region of the NACA 0018 airfoil at this time. In contrast, on the thinner NACA 0012 airfoil, another DSV seems to be growing. The above comparison suggests that, during a cycle of VAWT operation, the dynamic stall tends to occur later as the airfoil thickness increases.

Furthermore, the initiation time $t_1$ and detachment time $t_2$ of the initial dynamic stall vortex in a complete revolution cycle were independently calculated for the NACA 0012 and NACA 0018 airfoils using predefined criteria outlined in the preceding section. These values were then juxtaposed with the corresponding timings for the NACA 0015 airfoil, as presented in Table 2. Additionally, Table 2 includes the azimuth angle and effective angle of attack at these specific times for all three airfoils. Observing the transition from NACA 0012 to 0015 and 0018 airfoils, it is evident that the initiation time $t_1$ increases

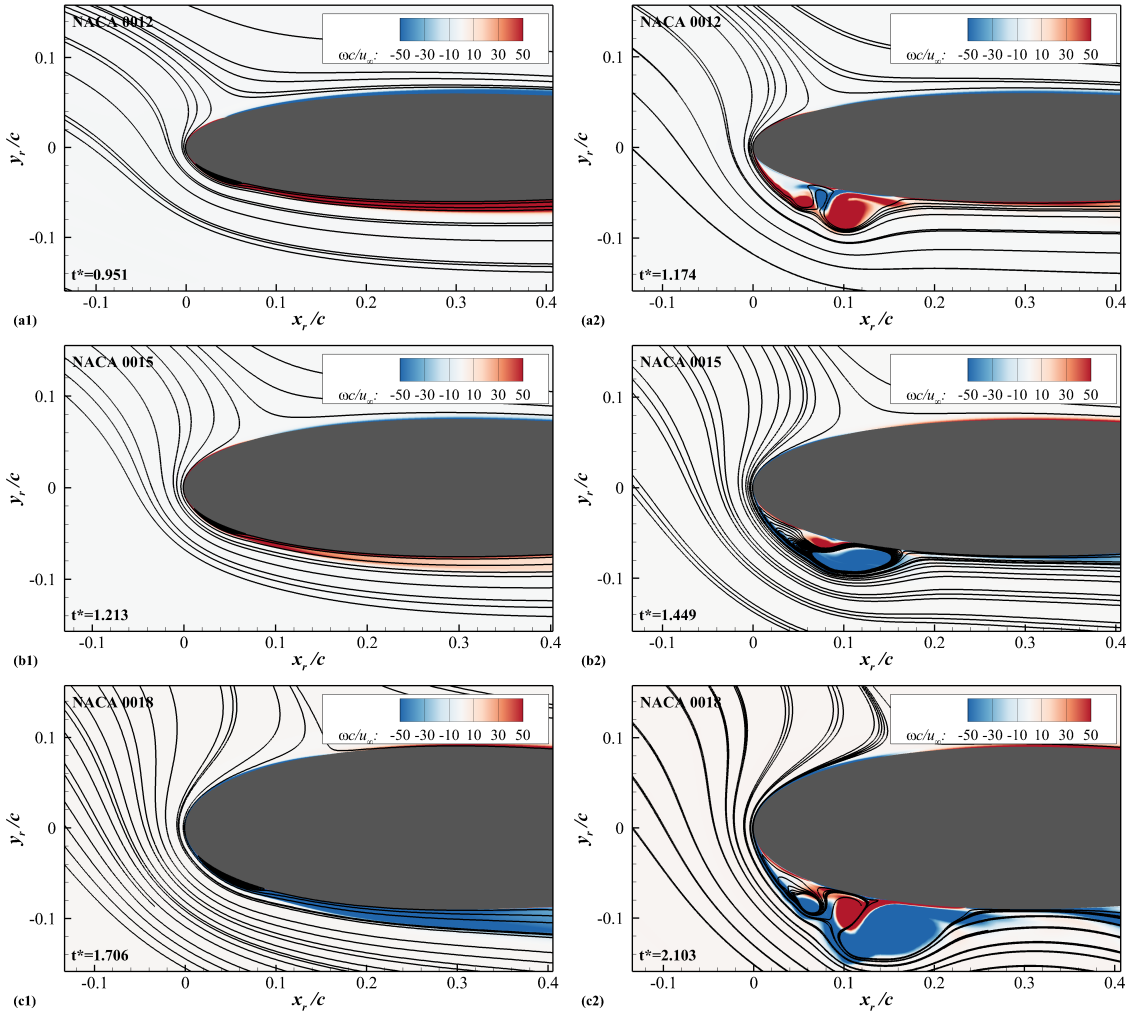


Figure 18: Transient vorticity fields at the initiation and detachment times of dynamic stall vortex for NACA 0012 (a1)-(a2), NACA 0015 (b1)-(b2) and NACA 0018 airfoil (c1)-(c2) airfoils, respectively.

from 0.951 to 1.121 and 1.706, respectively, while the detachment time $t_2$ increases from 1.174 to 1.449 and 2.103. This quantitative analysis substantiates the qualitative observation derived from Fig. 17, affirming that thicker airfoils have the capacity to delay both the initiation and detachment times of the DSV. Furthermore, Fig. 18 illustrates the instantaneous flow patterns at the initiation and detachment times of the DSV for the three airfoil profiles. Notably, as the airfoil thickness increases, the size of the DSV expands at both initiation and detachment times, particularly during the detachment phase. The thickness of the airfoil not only influences the temporal evolution of the DSV but also impacts the topology of the DSV.

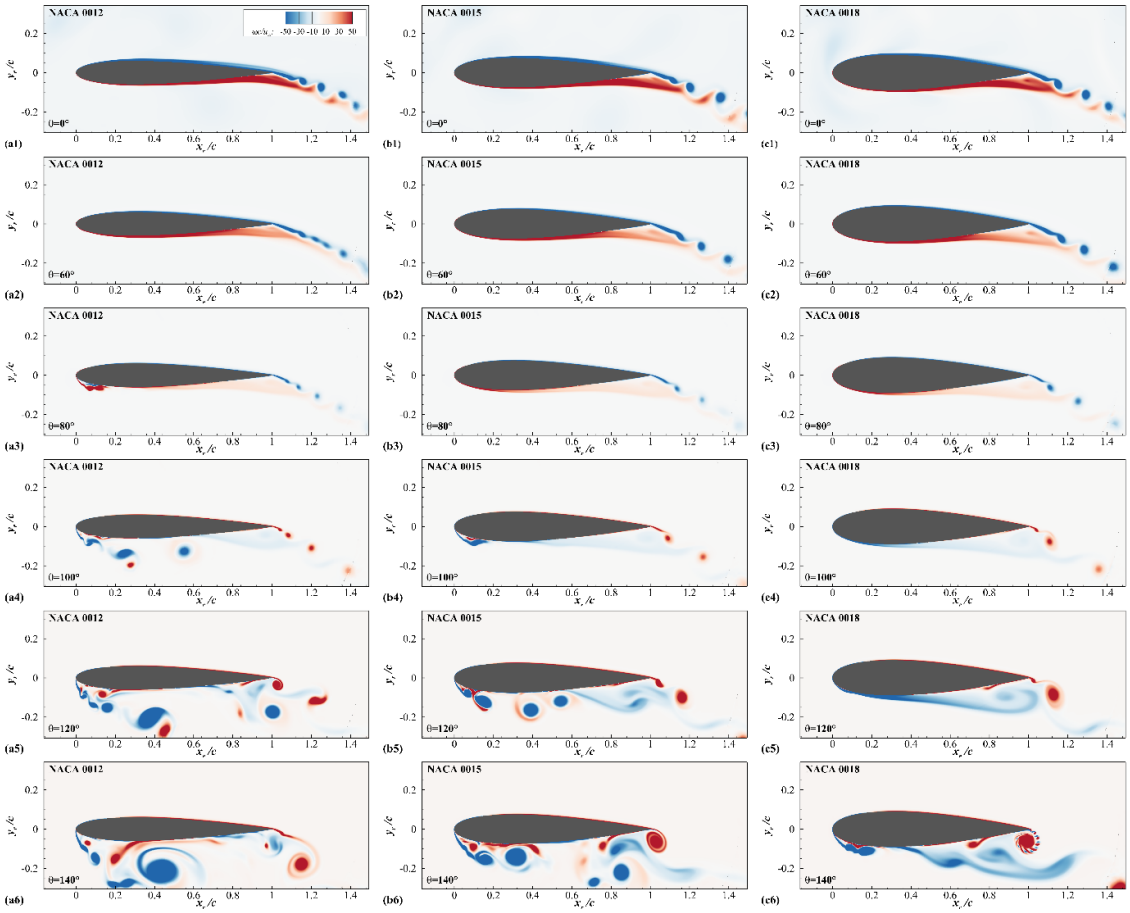


Figure 19: Transient vorticity fields of different airfoils at various azimuth angles. The left, middle and right columns correspond to the NACA 0012, 0015, 0018 airfoils, respectively.

Subsequently, the mechanism through which airfoil thickness affects the DSV is investigated. The transient flow fields at various azimuth angles in the initial half of a VAWT revolution cycle are displayed across the three columns of Fig. 19 for each of the three airfoils. Initially, consider the development of the DSV over the NACA 0012 airfoil. In the initial phase of a new VAWT revolution cycle starting from $\theta = 0°$, the flow on the

Table 2: The key parameters associated with DSV for three different airfoils.

| airfoil | $t_1$(s) | $\theta°$ | AoA(°) | $t_2$(s) | $\theta$(°) | AoA(°) |
|---|---|---|---|---|---|---|
| NACA 0012 | 0.951 | 65.40 | 20.621 | 1.174 | 80.70 | 24.539 |
| NACA 0015 | 1.213 | 83.40 | 25.159 | 1.449 | 99.60 | 28.273 |
| NACA 0018 | 1.706 | 117.36 | 29.966 | 2.103 | 144.60 | 26.054 |

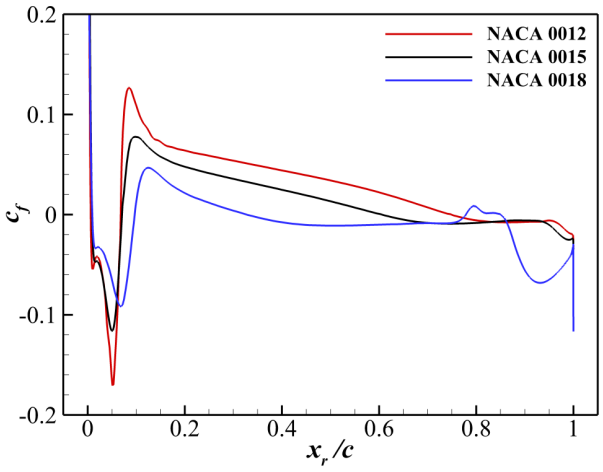


Figure 20: Wall friction coefficient curves on the suction side at the onset of dynamic stall for different airfoils.

suction side of the airfoil remains attached to the surface. With the increase of the airfoil's azimuth angle, separation and reversed flow become noticeable near the trailing edge, as illustrated in Fig. 19(a2) at $\theta = 60^\circ$. Further increments in the azimuth angle causes the emergence of a small laminar separation bubble at the leading edge, succeeded by the initiation and growth of the DSV, along with the upstream movement of the TE flow separation. This progression is depicted in Fig. 19(a3) at $\theta = 80^\circ$. At $\theta = 100^\circ$, the initial DSV has already detached, and the merging of LE flow separation with the upstream-moving TE flow separation leads to substantial flow separation over the suction surface of the airfoil, as shown in Fig. 19(a4). As the azimuth angle increases further to 120° and 140°, the flow separation over the airfoil intensifies and becomes more intricate, marked by the formation and shedding of new DSVs, as illustrated in Figs. 19(a5)-(a6). For the current NACA 0012 airfoil, given its small LE radius, an increase in the airfoil's azimuth angle tends to induce separation from the airfoil's leading edge under the influence of unfavorable pressure gradients. The resulting DSV originates from this leading-edge separation, and this type of stall is referred to as LE stall.

As depicted in the second column of Fig. 19, the flow evolution associated with NACA 0015 airfoil is similar to that of NACA 0012 model. Nevertheless, in the case of the NACA 0018 airfoil depicted in the third column of Fig. 19, the flow dynamics are notably distinct. As the azimuth angle increases, flow separation initially takes place at the TE region, as illustrated in Figs. 19(c1)-(c4). In contrast to the cases of NACA 0012 and 0015 airfoils, LE flow separation does not occur spontaneously but is instead induced by the upstream movement of the TE flow separation. This phenomenon is clearly observed in Fig. 19(c5) at $\theta = 120^\circ$, where the DSV is just initiated under the influence of the upstream-moving TE flow separation. Another observed difference is that the flow separation over the NACA 0018 airfoil is less severe than that associated with the two

thinner airfoils. The stall related to the thick airfoil is referred to as TE stall. Clearly, as the airfoil thickness increases, the nature of dynamic stall transitions from leading edge stall to trailing edge stall.

Fig. 20 presents the wall friction coefficient curves on the suction side at the onset of dynamic stall for three airfoils. The chart reveals that for the NACA 0012 and NACA 0015 airfoils, the changes in the friction coefficient (cf) at the beginning of dynamic stall primarily occur at the leading edge, marked by the first inflection point appearing in the negative cf region. However, for the NACA 0018 airfoil, this change is also accompanied by variations in cf at the trailing edge, indicating that separation occurs at the trailing edge as well. This more clearly demonstrates that the mechanism of dynamic stall changes with the variation in airfoil thickness.

### 3.3 Influence of airfoil thickness on efficiency of VAWT

In this section, the influence of airfoil's thickness on the efficiency of the VAWT is examined. The torque coefficient ($C_Q$) is employed to assess the aerodynamic efficiency of the VAWT with different blade cross-sections. The variation of $C_Q$ with azimuth angle is illustrated for a single blade and the entire VAWT system with two blades in Figs. 21(a)-(b), respectively. With a fixed tip speed ratio of 2, three blade cross-sections are considered: NACA0012, NACA0015, and NACA0018 sections. Evidently, the airfoil thickness exerts a significant influence on the efficiency of the VAWT. The data for both the individual blade and the entire VAWT system indicates that a higher airfoil thickness correlates with a higher instantaneous moment coefficient, signifying enhanced aerodynamic performance.

However, in this study, the better performance and efficiency of thick airfoils compared to thin airfoils is not solely due to their larger contact area. Another contributing

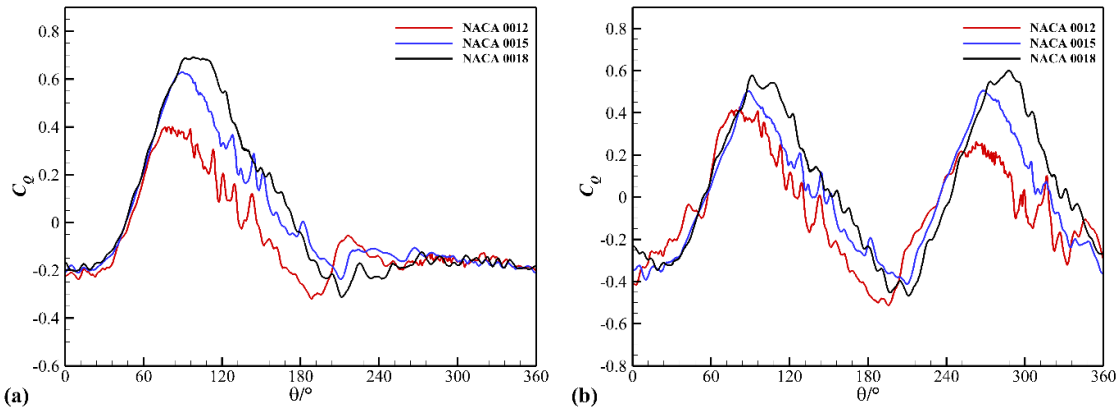


Figure 21: Comparison of instantaneous moment coefficients among three blade cross-sections. Plots (a) and (b) correspond to a single blade and the entire VAWT system with two blades.

factor is the delay in dynamic stall onset and changes in the mechanisms of dynamic stall induced by the thickness of the airfoils. Leading edge vortices are the main cause of power loss in vertical axis wind turbines. Thin airfoils, because of their small leading edge radius, provide an unfavorable curvature for the flow at a sufficiently high azimuth angle, so they are easily caused at the leading edge: the formation and rupture of laminar separation bubbles then form dynamic stall vortices. For thick airfoils, due to the unfavorable pressure gradient in the trailing edge area, the separation point moves from the trailing edge to the front edge, thus covering the entire suction surface of the airfoil. This will make the suction loss near the leading edge very slow and smooth. Therefore, the impact of dynamic stall will decrease as the airfoil thickness increases. This can also be seen from the instantaneous moment coefficient comparison chart in the Fig. 21. As the airfoil thickness increases, during the period when dynamic stall occurs, the moment coefficient fluctuates. slowing shrieking. Therefore, the delayed onset of dynamic stall and the transition from leading edge stall to trailing edge stall will improve the performance and efficiency of vertical axis wind turbines with different blade thicknesses.

Therefore, to improve the efficiency of wind energy utilization in wind turbines operating under various conditions, it is crucial to take into account the blade thickness.

## 4 Conclusions

The airflow surrounding a VAWT is primarily influenced by dynamic stall on the turbine blades. Given this background, this study delves into the numerical investigation of dynamic stall occurring on the blades of a VAWT system. Throughout dynamic stall, distinct flow structures imprint corresponding pressure patterns on the airfoil surface as they evolve. Extracting rich information from these signatures aids in comprehending flow development and predicting crucial flow events. In this study, to quantify dynamic stall, four key indicators, SDCP, HCMP, LPP, and MLPP, initially developed for predicting flow events associated with the DSV over an oscillating airfoil with finite pitching amplitude, are extended for the analysis of a VAWT system. Pressure data on the airfoil's suction surface are gathered to calculate these indicators. Accurate prediction of the onset of DSV in a VAWT revolution cycle is achieved by applying the SDCP and LPP criteria. Furthermore, detachment can be forecasted using the LPP and MLPP criteria. These indicators serve as quantitative metrics for pinpointing the commencement and separation of DSV, contributing to a more profound comprehension of distinct flow stages during dynamic stall evolution. Additionally, these indicators aid in elucidating the impact of geometric parameters of VAWTs on dynamic stall and the underlying flow mechanisms.

Concurrently, the study explores the impact of blade thickness on dynamic stall. The investigation reveals that, during the operation of a VAWT, an increase in airfoil thickness correlates with a delayed occurrence of dynamic stall. Furthermore, the mechanisms governing the occurrence of dynamic stall differ. In the case of the thin NACA 0012 airfoil, the small leading-edge radius makes the flow susceptible to separation from the leading

edge as the airfoil's azimuth angle increases. Consequently, this type of stall is referred to as LE stall. The dynamic stall evolution observed with the NACA 0015 airfoil is similar to that of the NACA 0012 model. In contrast, for the thick NACA 0018 airfoil, the initial flow separation occurs at the TE region. As the azimuth angle increases, the separation point gradually shifts from the TE region toward the LE, progressively encompassing a significant portion of the blade's suction surface. This flow reversal eventually extends to the LE, inducing the formation of DSV. Therefore, the dynamic stall associated with the thick airfoil is commonly referred to as TE stall.

Lastly, the investigation delves into the influence of blade thickness on the aerodynamic performance of VAWT. The findings reveal a consistent trend across the NACA 0012, NACA 0015, and NACA 0018 airfoils: as the airfoil thickness increases, there is a corresponding rise in the moment coefficient, signifying enhanced wind energy utilization efficiency. This underscores the significance of airfoil thickness in wind turbine design and suggests that there might be an optimal blade thickness for the aerodynamic performance optimization of each specific wind turbine.

## References


[1] S. Roy and U. Saha, *Wind tunnel experiments of a newly developed two-bladed Savonius-style wind turbine,* Appl. Energy, 137 (2015), pp. 117–125.

[2] N. Ma and H. Lei et al., *Airfoil optimization to improve power performance of a high-solidity vertical axis wind turbine at a moderate tip speed ratio,* Energy, 150 (2018), pp. 236–252.

[3] Q. Li, Z. Shu and F. Chen, *Performance assessment of tall building-integrated wind turbines for power generation,* Appl. Energy, 165 (2016), pp. 777–788.

[4] A. Yang, and Y. Su et al., *Estimation of wind power generation in dense urban area,* Appl. Energy, 171 (2016), pp. 213–230.

[5] M. Islam, S. Mekhilef and R. Saidur, *Progress and recent trends of wind energy technology,* Renewable and Sustainable Energy Rev., 21 (2013), pp. 456–468.

[6] W. Hao, M. Bashir, C. Li and C. Sun, *Flow control for high-solidity vertical axis wind turbine based on adaptive flap,* Energy Conversion and Management, (2021), 249.

[7] K. Gompertz and C. Jensen et al., *Modification of transonic blowdown wind tunnel to produce oscillating freestream Mach number,* AIAA J., 49(11) (2011), pp. 2555–2563.

[8] S. Benton and M. Visbal, *Effects of leading-edge geometry on the onset of dynamic stall,* AIAA J., 56(10) (2018), pp. 4195–4198.

[9] A. Sharma and M. Visbal, *Numerical investigation of the effect of airfoil thickness on onset of dynamic stall,* J. Fluid Mech., 870 (2019), pp. 870–900.

[10] P. Ouro, T. Stoesser and L. Ramírez, *Effect of blade cambering on dynamic stall in view of designing vertical axis turbines,* J. Fluids Eng., 140(6) (2018).

[11] J. Zheng, and Y. Cui, et al., *Investigation of airfoil leading edge separation control with nanosecond plasma actuator,* Phys. Rev. Fluids, 1 (2016).

[12] A. Rezaeiha, I. Kalkman and B. Blocken, *CFD simulation of a vertical axis wind turbine operating at a moderate tip speed ratio: Guidelines for minimum domain size and azimuthal increment,* Renewable Energy, 107 (2017), pp. 373–385.

[13] Q. LI, T. MAEDA,Y. KAMADA AND J. MURATA ET AL., *Wind tunnel and numerical study of a straight-bladed vertical axis wind turbine in three-dimensional analysis (Part I: for predicting aerodynamic loads and performance),* Energy, 106 (2016), pp. 443–452.
[14] G. TESCIONE, C. RAGNI, C. FERREIRA AND G. BUSSEL, *Near wake flow analysis of a vertical axis wind turbine by stereoscopic particle image velocimetry,* Renewable Energy, 70 (2014), pp. 47–61.
[15] T. CORKE AND F. THOMAS, *Dynamic stall in pitching airfoils: aerodynamic damping and compressibility effects,* Ann. Rev. Fluid Mech., 47(1) (2015), pp. 479–505.
[16] X. LI AND L. FENG, *Critical indicators of dynamic stall vortex,* J. Fluid Mech., 937 (2022), A16.
[17] S. NARSIPUR, P. HOSANGADI, A. GOPALARATHNAM AND J. EDWARDS, *Variation of leading-edge suction during stall for unsteady aerofoil motions,* J. Fluid Mech., 900 (2020), A25.
[18] N. BENARD, L. CATTAFESTA, E. MOREAU, J. GRIFFIN AND J. BONNET, *On the benefits of hysteresis effects for closed-loop separation control using plasma actuation,* Phys. Fluids, 23(8) (2011).